LARGE-SCALE THREE-DIMENSIONAL ACOUSTIC HORN OPTIMIZATION

STEPHAN SCHMIDT[†§] EDDIE WADBRO[‡] MARTIN BERGGREN[‡]

Abstract. We consider techniques that enable large-scale gradient-based shape optimization of wave-guiding devices in the context of 3D time-domain simulations. The approach relies on a memory efficient boundary representation of the shape gradient together with primal and adjoint solvers semi-automatically generated by the FEniCS framework. The hyperbolic character of the governing linear wave equation, written as a first-order system, is exploited through systematic use of the characteristic decomposition both to define the objective function and to obtain stable numerical fluxes in the Discontinuous Galerkin spatial discretization. The methodology is successfully used to optimize the shape of midrange acoustic horns for maximum transmission efficiency.

Key words. Shape Optimization, Shape Derivatives, Acoustic Wave Equation, Computational Acoustics, Discontinuous Galerkin Method, Code Generation

AMS subject classifications. 35L05, 65K10, 65M25, 65M32, 68N19

1. Introduction.

Horn-like structures appear in devices for both acoustic and electromagnetic waves. A horn serves as an interface between a waveguide or a radiation source and the surrounding space and provides both impedance matching to the source and directivity control of the transmission. These properties are utilized in a variety of applications. The *bell* in brass instruments constitutes a part of a resonator—the air space within the instrument—and the bell shape is judiciously designed to constrain the most important resonances to integer frequency ratios. Recently, there have been some efforts to use numerical shape optimization in order to design brass bells so that the instrument acquires prescribed resonance characteristics [8, 21]. A type of acoustic *inverse horn*, that is, a device that possesses a large diameter at the source and a small at the outlet, is used in Ultrasonic Machining, a subtractive manufacturing process particularly suitable for hard and brittle materials [1]. Horn *loudspeakers*, which are at focus here, are routinely applied for the mid- and high-frequency range in public address systems for large halls, cinemas, and outdoors, often assembled in the form of so-called line arrays [35]. A horn dramatically raises the efficiency of the radiating source and may be used for precise directional control of the coverage area. In spite of its advantages, horn-equipped loudspeakers are often viewed as subpar with respect to sound quality [10, § 4.9]. However, some of the sound-quality deficiencies of horns may be due to suboptimal design and not to inherent limitations of the concept of acoustical horns.

The classical analysis of wave motion in horns, based on the 1D Webster horn equation [20], is rapidly being complemented with more accurate numerical methods. During the last decade or so, a number of studies have appeared that use optimization algorithms together with numerical solutions of the governing equation to design acoustic horns [3, 4, 6, 13, 17, 32, 33]. It turns out that detailed shaping of the horn flare by using numerical shape optimization methods can produce horns with very favorable input impedance properties, as also has been confirmed by measurements on manufactured prototypes [22]. Some studies consider the directivity properties of the horn in the optimization process [19, 31, 34] instead of, or in addition to the

[†]Department of Mathematics, University of Würzburg, 970 74 Würzburg, Germany
[‡]Department of Computing Science, Umeå University, SE–901 87 Umeå, Sweden
[§]Corresponding author email: (stephan.schmidt@mathematik.uni-wuerzburg.de)

input impedance. All the above mentioned studies employ frequency-domain modeling and are confined to 2D geometries, which means that only cylindrical (or laterally infinite) horns can be considered. However, in practice, it is important to be able to separately control the vertical and horizontal directivity properties, which will necessitate full 3D acoustic models. Moreover, since the radiation properties of horns ideally should be uniform throughout its operational range, frequency-domain methods need to be run at a large number of frequencies. It may therefore be beneficial to consider time-domain methods, where only one equation needs to be solved at each design cycle. The frequency content for which the horn should be optimized is then controlled by selecting a suitable input pulse.

In contrast to previous work, our aim here is to apply numerical shape optimization for *detailed design* of an acoustic horn in *full 3D* using a *time-domain model* of the acoustic wave propagation. We consider here only the impedance-matching aspect, setting the stage for future treatment of more complex problems, such as optimizing with respect to directivity properties. The linear wave equation written in first-order form models the wave propagation. The hyperbolic nature of the equations is respected through the use of a Discontinuous Galerkin spatial discretization with upwinding fluxes based on a characteristic decomposition [15]. The characteristic decomposition is also used to define the objective function.

Since we rely on gradient-based optimization and the adjoint-variable method for the sensitivity analysis, the computational complexity for each gradient evaluation is independent of the number of design variables. We use this property to be able to control the shape in detail; each mesh point on the horn's surface is subject to design, and a smoothing strategy is utilized to promote smooth design updates. For efficiency, both computationally and with respect to implementation effort and maintainability of the software, we make use of the FEniCS [18] suite to generate the primal solver for acoustic analysis. The corresponding discrete adjoint solver is then automatically generated by Dolfin-Adjoint [14]. The gradient expression used by the optimization routine is assembled from the primal and adjoint solutions using an expression derived from the equations in integral form. This approach yields a boundary-integral representation for the objective function gradient, which means that the gradient expression only requires the time history of the primal and adjoint solutions restricted to the design surface, and not everywhere in the computational domain, which would be extremely memory demanding for a time-domain calculation. The necessity to differentiate the mesh deformation procedure is likewise eliminated by this approach.

The paper is structured as follows. In Section 2, we review the governing equations and the concept of characteristic decomposition, which is central to this application. Sections 3 and 4 introduce the objective function and the resulting first-order optimality system. The discretization scheme is presented in Section 5 and results from cross-code verification studies are given in Section 6. Finally, Section 7 presents results of the optimization of two different acoustic horns in three dimensions.

2. Acoustic power balance and the characteristic decomposition. We use the concept of a *characteristic decomposition* of the acoustic power flux over surfaces extensively throughout the following. The concept, which is shortly reviewed in this section, is used to define physical boundary conditions, the objective function of optimization, and to specify inter-element fluxes in the numerical scheme.

Acoustic wave propagation in still air under the conditions of uniform static density

and temperature is governed by the linear wave equation

$$\frac{\partial u}{\partial t} + \nabla p = 0, \tag{2.1a}$$

$$\frac{\partial p}{\partial t} + c^2 \mathrm{div}\, u = 0, \tag{2.1b}$$

where p denotes the acoustic pressure, u the acoustic momentum density vector, that is, the product of the static air density and the acoustic velocity vector, and c the speed of sound.

For each open, bounded domain D in space, solutions to system (2.1) satisfy the conservation law

$$\frac{d}{dt}\frac{1}{2}\int_D \|u\|^2 + \frac{1}{c^2}p^2\, dx = -\int_{\partial D} p\langle u, n\rangle\, d\Gamma, \tag{2.2}$$

where n is the outward-directed unit normal on ∂D, $\langle\,\cdot\,,\,\cdot\,\rangle$ denotes the Euclidean inner product, and $\|u\|^2 = \langle u, u\rangle$. Conservation law (2.2) says that the time derivative of the acoustic energy in D equals the net flux of acoustic power[1] into D through boundary ∂D. Conservation law (2.2) is obtained by taking the dot product of equation (2.1a) with u, multiplying equation (2.1b) with p/c^2, summing the equations, integrating, and using the divergence theorem.

The integrand on the right side of conservation law (2.2) can be split up into a difference of two positive terms as follows,

$$\begin{aligned} -p\langle u, n\rangle &= \frac{1}{c}\left(\frac{1}{2}\left(p - c\langle u, n\rangle\right)\right)^2 - \frac{1}{c}\left(\frac{1}{2}\left(p + c\langle u, n\rangle\right)\right)^2 \\ &= \frac{1}{c}\left(w_-^2 - w_+^2\right), \end{aligned} \tag{2.3}$$

where

$$w_\pm = \frac{1}{2}\left(p \pm c\langle u, n\rangle\right) \tag{2.4}$$

are called the *characteristic variables*. By substituting the splitting (2.3) into conservation law (2.2), we find that

$$\frac{d}{dt}\frac{1}{2}\int_D \|u\|^2 + \frac{1}{c^2}p^2\, dx = \frac{1}{c}\int_{\partial D} w_-^2 - w_+^2\, d\Gamma, \tag{2.5}$$

which reveals that the use of characteristic variables yields a splitting of the power flux over ∂D into the acoustic power that flows *into* the domain D (integral of w_-^2) and the the power that flows *out* of the domain (integral of w_+^2). The plus and the minus subscripts in the characteristic variables indicate the direction in relation to the (outward-directed) normal n on ∂D.

[1] To obtain the correct dimensions of power, the terms in equation (2.2) should be divided with the static air density.

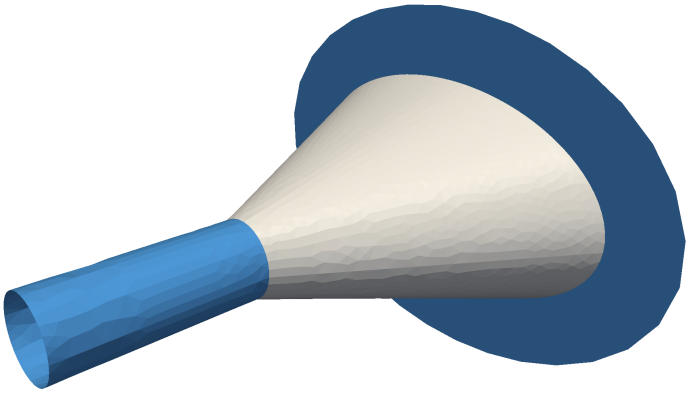

FIG. 3.1. *The geometry for the model problem comprises a horn that on one side is mounted in an infinite baffle and on the other side attached to a waveguide. Variable horn flare in light gray, fixed wave-guide and baffle in blue. Surrounding domain Ω not shown.*

3. The model problem. We consider the three dimensional setup illustrated in Figure 3.1. To reduce the computational cost, we will only compute on a quarter of the domain. This setup consists of a waveguide attached to the throat of an acoustic horn that is mounted in an infinite baffle. We denote by Γ_{wall} the sound-hard walls of the waveguide, the acoustic horn, and the baffle, and by Γ_{symm} the symmetry boundaries. For numerical reasons, we truncate the domain and denote the truncated computational domain by Ω. The boundary $\partial\Omega$ can be decomposed as the closure of $\Gamma_{\text{wall}} \cup \Gamma_{\text{symm}} \cup \Gamma_{\text{in}} \cup \Gamma_{\text{out}}$, where the two latter parts stem from the truncation of the computational domain. More precisely, Γ_{in} truncates the waveguide and Γ_{out} is the boundary that truncates the free-space in front of the horn. The acoustic initial–boundary-value problem we consider is

$$
\begin{aligned}
\frac{\partial u}{\partial t} + \nabla p &= 0 \quad \text{in } \Omega, \text{ for } t > 0,\\
\frac{\partial p}{\partial t} + c^2 \operatorname{div} u &= 0 \quad \text{in } \Omega, \text{ for } t > 0,\\
\frac{1}{2}\left(p - c\langle u, n\rangle\right) &= g \quad \text{on } \Gamma_{\text{in}}, \text{ for } t > 0,\\
\frac{1}{2}\left(p - c\langle u, n\rangle\right) &= 0 \quad \text{on } \Gamma_{\text{out}}, \text{ for } t > 0,\\
\langle u, n\rangle &= 0 \quad \text{on } \Gamma_{\text{wall}} \cup \Gamma_{\text{symm}}, \text{ for } t > 0,\\
u &\equiv 0 \quad \text{in } \Omega, \text{ at } t = 0,\\
p &\equiv 0 \quad \text{in } \Omega, \text{ at } t = 0,
\end{aligned}
\tag{3.1}
$$

where g is a given function with compact support in time. From the discussion in Section 2, we see that the boundary condition on Γ_{in} sets the incoming characteristic (w_-) to be equal to the given function g, and the boundary condition on Γ_{out} ensures that no incoming acoustic power is transmitted into Ω from the exterior. The condition of a sound hard material is imposed through the boundary condition on Γ_{wall}. The zero normal velocity condition also imposes the symmetry condition at Γ_{symm}.

Applying the power balance law (2.5) on solutions to system (3.1) under the

specified boundary conditions, we find that

$$\frac{d}{dt}\frac{1}{2}\int_\Omega \|u\|^2 + \frac{1}{c^2}p^2\,dx = \frac{1}{c}\int_{\Gamma_{\text{in}}} g^2 - w_+^2\,d\Gamma - \frac{1}{c}\int_{\Gamma_{\text{out}}} w_+^2\,d\Gamma, \tag{3.2}$$

where we have made use of the characteristic variables as defined in expression (2.4).

Since we assume that the input g has compact support in time, it holds for an "open" system like this one that the solution will vanish identically after a sufficiently long time T, which is consistent with the fact that the right side of conservation law (3.2) becomes negative when $g \equiv 0$. Thus, integrating expression (3.2) over a sufficiently long time interval $(0, T)$, utilizing the initial condition $u(0) = 0$ and $p(0) = 0$ and the vanishing assumption $u(T) = 0$ and $p(T) = 0$, we find that

$$\int_0^T\int_{\Gamma_{\text{in}}} g^2\,d\Gamma = \int_0^T\int_{\Gamma_{\text{in}}} w_+^2\,d\Gamma + \int_0^T\int_{\Gamma_{\text{out}}} w_+^2\,d\Gamma. \tag{3.3}$$

Expression (3.3) states the basic energy balance of system (3.1): the total acoustic energy of the input signal (left side) equals the energy of the reflected signal (first term on right side) plus the energy transmitted to the surroundings (the second term on the right side). Thus, to maximize the total transmitted energy, we may equivalently minimize the reflected signal, which will be simpler to do in a numerical implementation.

Here, we let the shape of boundary Γ_{horn}, colored light gray in Figure 3.1, be subject to design. The beginning and the end of the horn flare will be fixed, so that the optimization neither can change the mouth and throat shapes nor the length of the horn. Each such admissible horn shape will generate a candidate computational domain Ω, for which we solve state equation (3.1) and evaluate the objective function

$$J(\Omega) = \frac{1}{2}\int_0^T\int_{\Gamma_{\text{in}}} \left(p + \langle u, n\rangle\right)^2\,d\Gamma\,dt, \tag{3.4}$$

integrated for a sufficiently long time T with respect to the time support of the input signal g. The optimization problem can then be formulated

$$\begin{aligned} &\min J(\Omega) \text{ subject to} \\ &\text{state equation (3.1).} \end{aligned} \tag{3.5}$$

If the final design is such that the objective function, that is, the reflected signal, vanishes for the given input signal, then the *input impedance* at the throat of the horn is real and constant for each of the frequencies contained in the signal. (For a discussion of the relation between reflections, which is the measure we use here, and the concept of acoustic impedance, we refer to the acoustics literature, for instance Rienstra & Hirschberg's lecture notes [23, § 3.2].) This approach is appropriate for transmission optimization of a horn in isolation, as here. However, if a model of the wave source, typically a *compression driver* in the case of a mid- or high-frequency horn, is available, it would also be possible to maximize the total transmitted acoustic power for the coupled system driver–horn.

4. Domain variations and optimality system. Conceptually, design problem (3.5) is a PDE-constrained optimization problem with the added difficulty that there is a need to associate with the shape of Γ_{horn} a suitable set of decision variables in the optimization algorithm. There are several possible choices. One possibility is to introduce an artificial inhomogeneous static density function into the governing equations, so that regions of sound-hard materials are approximated using a dense fluid. This approach transforms the problem from one using a varying domain to one that involves a variable coefficient in the governing equations [5, 28, 33]. Another possibility is to use an explicit parameterization of feasible domain shapes through, for instance, a finite set of smooth ansatz functions [16]. Here, we consider domain deformations that are assumed to be generated by a sufficiently smooth vector field $V : \mathbb{R}^3 \to \mathbb{R}^3$. This approach can be exploited to derive a computationally efficient boundary representation of the shape derivative, a property related to the so-called Hadamard–Zolésio structure theorem [11, 29].

A boundary representation of the shape gradient allows for very efficient numerical schemes utilizing the maximum degrees of freedom by exercising the position of every surface vertex as a design parameter. Furthermore, all terms stemming from a deformation of the mesh and those related to the differentiation of the PDE solution procedure with respect to the input mesh are treated on an analytic level, thereby circumventing the need to actually compute them on a discrete level. The resulting methodology is independent of the actual PDE solver and the sensitivities can be computed using any methodology to solve the state equation, provided an adjoint is also available. The applicability of this approach to large-scale three dimensional problems in aerodynamics was for example considered previously in [26].

The appendix carries out the shape sensitivity analysis for optimization problem (3.5) with state equation (3.1) written in an suitable integral form. To obtain the final boundary representation for the shape derivative, quite delicate conditions on the regularity of the solution have to be assumed, as indicated in the appendix. Such high regularity does not hold for typical finite-element functions, which means that the boundary representation of the shape derivative as derived in the appendix will not be fully consistent with a differentiation of the objective function actually used after discretization [7], [11, Remark 2.3].

For the studied problem, the admissible shape changes of Γ_{horn} are generated through a smooth vector field $V : \mathbb{R}^3 \to \mathbb{R}^3$ that vanishes everywhere on $\partial\Omega$ except on Γ_{horn}. After a sensitivity analysis as outlined in the Appendix, we find that the shape derivative of objective function (3.4) with respect to V has the boundary representation

$$dJ(\Omega)[V] = c \int_0^T \int_{\Gamma_{\text{horn}}} \langle V, n\rangle \,\text{div}\,(up^*)\, d\Gamma\, dt, \tag{4.1}$$

where u solves system (3.1) and p^* the adjoint system

$$\begin{aligned}
-\frac{\partial u^*}{\partial t} + \nabla p^* &= 0 && \text{in } \Omega, \text{ for } t < T,\\
-\frac{\partial p^*}{\partial t} + c^2 \text{div}\, u^* &= 0 && \text{in } \Omega, \text{ for } t < T,\\
\frac{1}{2}\left(p^* - c\langle u^*, n\rangle\right) &= \frac{1}{2}\left(p + c\langle u, n\rangle\right) && \text{on } \Gamma_{\text{in}}, \text{ for } t < T,\\
\frac{1}{2}\left(p^* - c\langle u^*, n\rangle\right) &= 0 && \text{on } \Gamma_{\text{out}}, \text{ for } t < T,
\end{aligned} \tag{4.2}$$

$$\begin{aligned} \langle u^*, n\rangle &= 0 && \text{on } \Gamma_{\text{wall}} \cup \Gamma_{\text{symm}}, \text{ for } t < T, \\ u^* \equiv 0, \qquad p^* &\equiv 0 && \text{in } \Omega, \text{ at } t = T, \end{aligned}$$

We note that the adjoint system (4.2) after the variable change $t \mapsto T - t$ equals the state equation (3.1) with $w_+(T-t)|_{\Gamma_{\text{in}}}$ instead of $g(t)$ as source. That is, the state and adjoint systems are the same, but the state equation is driven by the given source function g and the adjoint equation by the time convolution of the reflected signal at the inlet.

5. Spatial Discretization. To introduce the variational form that is the basis for our Discontinuous Galerkin discretization, we consider an open, bounded and connected set $K \subset \Omega$, representing what later will be an element in our triangulation. Assume that u and p satisfy system (3.1). Multiplying the first and second equations in system (3.1) with arbitrary smooth test functions v and q, respectively, integrating over K, and integrating by parts in space, we find that $u(t)|_K$ and $p(t)|_K$ satisfy

$$\int_K \langle v, \partial_t u\rangle - p \operatorname{div} v + q\, \partial_t p - c^2\langle u, \nabla q\rangle \, dx + \int_{\partial K} \langle v, n\rangle p + c^2 \langle u, n\rangle q \, d\Gamma = 0, \tag{5.1}$$

for each pair of smooth test functions v and q with support in K. Next, we introduce the *flux functions*

$$\begin{aligned} f_1(u, p, n) &:= np = n(w_+ + w_-) \\ f_2(u, p, n) &:= c\langle u, n\rangle = (w_+ - w_-) \end{aligned} \tag{5.2}$$

which, as we see above, can be written in terms of sums and differences of the characteristic variables (2.4), a property that will be exploited below to define the numerical flux functions. Using definitions (5.2), equation (5.1) can be written as

$$\int_K \langle v, \partial_t u\rangle - p \operatorname{div} v + q\, \partial_t p - c^2\langle u, \nabla q\rangle \, dx + \int_{\partial K} \langle v, f_1\rangle \; + c\, q f_2 \, d\Gamma = 0. \tag{5.3}$$

Now introduce a triangulation $\mathscr{T}_h$ of the domain Ω consisting of non-overlapping open tetrahedrons K such that $\overline{\Omega} = \cup_{K\in\mathscr{T}_h} \overline{K}$. The numerical scheme is defined by requiring that $p(t)$ and the components of vector $u(t)$ are functions whose restrictions on each K are polynomials that satisfy a modified version of variational expression (5.3) for all polynomial test functions v and q. Since p and u will then in general possess jump discontinuities over each interface between two neighboring elements, the question is what values to use in the flux functions f_1, f_2, since they are evaluated exactly where the functions are discontinuous. A standard choice that leads to a consistent and stable scheme is *upwinding*. This method exploits the directivity information in the characteristic variables and use the *local* values in K in the *outgoing* characteristic variable w_+, and the *remote* values —from neighboring cells or from the boundary conditions— in the *incoming* characteristic variable w_-. More precisely, let $\mathcal{P}_r$ define the space of polynomials of maximum degree r. For each $K \in \mathscr{T}_h$, we require $u(t)|_K \in P_r^3$, $p(t)|_K \in P_r$ such that for each $v \in P_r^3$, $q \in P_r$,

$$\int_K \langle v, \partial_t u\rangle - p \operatorname{div} v + q\, \partial_t p - c^2\langle u, \nabla q\rangle \, dx + \int_{\partial K} \langle v, f_1^*\rangle \; + c\, q f_2^* d\Gamma = 0, \tag{5.4}$$

where the *upwind numerical flux functions* are defined by

$$\begin{aligned} f_1^* &:= n(w_+^L + w_-^R) = n\left[\frac{1}{2}\left(p^L + p^R\right) + \frac{c}{2}\left(\langle u^L, n\rangle - \langle u^R, n\rangle\right)\right], \\ f_2^* &:= w_+^L - w_-^R = \frac{1}{2}\left(p^L - p^R\right) + \frac{c}{2}\left(\langle u^L, n\rangle + \langle u^R, n\rangle\right), \end{aligned} \tag{5.5}$$

where the superscripts L and R denotes local and remote values. The local values are given by the values of $u|_K$ and $p|_K$ on ∂K. The remote values are either given in order to assign boundary conditions, if ∂K coincides with the boundary, or by the values of $u|_{K'}$ and $p|_{K'}$, if there is a neighboring $K' \in \mathscr{T}_h$ such that $\overline{K'} \cap \overline{K} \subset \partial K$, that is, we are at a face that is shared between K and K'. The term "upwind" for the flux function (5.5) is borrowed from fluid mechanics and is motivated by the fact that the characteristic variables are evaluated according the direction of power transport across ∂K.

By imposing the remote states

$$\begin{aligned} u^R &:= -\frac{1}{c} g n, \quad p^R := g \quad \text{on } \Gamma_{\text{in}}, \\ u^R &:= 0, \qquad\quad p^R := 0 \quad \text{on } \Gamma_{\text{out}}, \end{aligned} \tag{5.6}$$

we see that the incoming characteristic w_-^R on Γ_{in} and Γ_{out} will be set to the correct values as specified by system (3.1).

Since we only compute on a quarter of the horn, we impose that the solution should be symmetric across planes Γ_{symm}. The symmetry and sound hard boundary condition $\langle u, n\rangle = 0$ is here imposed by the custom numerical flux function

$$f_{1,\text{ws}}^* = n p^L, \qquad f_{2,\text{ws}}^* = 0, \tag{5.7}$$

which can be motivated by substituting condition $\langle u, n\rangle = 0$ into the exact flux functions (5.2). An alternative strategy to impose condition $\langle u, n\rangle = 0$ is to use the upwind flux (5.5) and specify a remote state that mirrors the local state according to the formula $u^R := u^L - 2\langle u^L, n\rangle n$ and $p^L := p^R$ on Γ_{symm}. However, in the numerical experiments below, we have chosen the explicit wall flux function (5.7), since this choice will lead to a boundary integral over Γ_{horn} in the variational form whose integrand is *linear* in the wall normal. This property is consistent with the choice made to enforce the wall boundary condition in the integral form used for sensitivity analysis, equation (A.10), and leads to a much simpler expression for the shape gradient compared to the case when mirroring the local state; see the discussion in § A.1.

To specify the complete scheme, based the discussion above, we need a number of definitions. Let $S = \cup_{k=1}^M S_m$ be the union of all open triangular element faces S_m that are shared between two elements, that is, the set of element faces that are not part of the boundary. For each such internal element face S_m, it holds that $\overline{S}_m = \partial K_{m_1} \cap \partial K_{m_2}$ for some distinct neighboring elements K_{m_1}, $K_{m_2} \in \mathcal{T}_h$. We denote by n_{m_1}, $n_{m_2} = -n_{m_1}$ the outward-directed unit normals to K_{m_1} and K_{m_2} on S_m. For each piecewise-polynomial f, we define $f_1 = f|_{K_{m_1}}$, $f_2 = f|_{K_{m_2}}$ and the face-sum and face-jump operators

$$\begin{aligned} \{\!\{ f \}\!\} &:= f_1|_{S_m} + f_2|_{S_m}, \\ [\![f]\!] &:= \begin{cases} n_{m_1} f_1|_{S_m} + n_{m_2} f_2|_{S_m} & \text{if } f \in \mathbb{R}, \\ \langle n_{m_1}, f_1|_{S_m}\rangle + \langle n_{m_2}, f_2|_{S_m}\rangle & \text{if } f \in \mathbb{R}^3. \end{cases} \end{aligned} \tag{5.8}$$

Moreover, we define $\Omega_0 := \Omega \setminus \overline{S}$ and the function

$$\hat{g} := \begin{cases} g & \text{on } \Gamma_{\text{in}}, \\ 0 & \text{on } \Gamma_{\text{out}}. \end{cases} \tag{5.9}$$

Now we sum equation (5.4) over all $K \in \mathscr{T}_h$, utilizing the upwind flux (5.5) over the element interfaces, imposing the remote states (5.6) and the wall/symmetry fluxes (5.7). We then obtain that $u(t) \in P_r^3(\mathscr{T}_h)$, $p(t) \in P_r(\mathscr{T}_h)$ satisfy

$$\begin{aligned} &\int_{\Omega_0} \langle v, \partial_t u \rangle - p \operatorname{div} v + q\, \partial_t p - c^2 \langle u, \nabla q \rangle \, dx + \int_{\Gamma_{\text{wall}} \cup \Gamma_{\text{symm}}} \langle v, np \rangle \, d\Gamma \\ &+ \int_{\Gamma_{\text{in}} \cup \Gamma_{\text{out}}} \big\langle v, n\big[\hat{g} + \frac{1}{2}(p + c\langle u, n\rangle)\big]\big\rangle + cq\big[\frac{1}{2}(p + c\langle u, n\rangle) - \hat{g}\big] \, d\Gamma \\ &\qquad + \frac{1}{2}\int_S [\![v]\!]\big(\{\!\{\, p \,\}\!\} + c[\![u]\!]\big) \, d\Gamma + \frac{1}{2}\int_S c\big\langle [\![q]\!], \big([\![p]\!] + c\{\!\{\, u \,\}\!\}\big)\big\rangle \, d\Gamma = 0, \end{aligned} \tag{5.10}$$

for each $v \in P_r^3(\mathscr{T}_h)$, $q \in P_r(\mathscr{T}_h)$.

6. Implementation and verification. Variational problem (5.10) is implemented numerically using the FEniCS environment [18], which contains a domain specific language for variational problems. After postulating the variational expression in Python, a C/C++ discontinuous Galerkin solver of desired spatial order is automatically generated and compiled by the FEniCS environment. Time derivatives are discretized by the trapezoidal method. (A completely explicit low storage fourth order Runge–Kutta scheme is also implemented, but this scheme behaves problematically if the mesh quality degrades too much during shape optimization when the mesh is deformed.) The implicit equation to solve for each time-step is linear. Depending on available compute power, spatial order, and mesh refinement, we first attempt to factorize the system once and store this factorization for all time-steps. If this is not tractable, for example due to excessive storage requirements, we solve the implicit equation for each time-step using restarted GMRES with ILU preconditioning, a functionality provided by PETSc and Hypre.

In frequency domain, a horn's radiation efficiency can be characterized by its *reflection coefficient* at the throat, which for each frequency measures the (complex-valued) quotient between the pressure amplitude of an incoming single frequency wave and the reflected wave's pressure amplitude. To verify our implementation, we compute the reflection coefficient spectrum with our code as well as with Comsol Multiphysics on the cylindrically symmetric domain illustrated in Figure 6.1. Here, the width and length of the waveguide are set to $a = 19.3$ mm and $d = 100$ mm, respectively. This geometry corresponds to a cross-section of one of the three dimensional problems considered later. The length of the conical horn flare is $l = 150$ mm and the half width of the horn mouth is $b = 100$ mm. For all simulations, the speed of sound is $c = 345$ m/s.

The baseline for the verification computations are carried out with Comsol in frequency domain. That is, we consider single-frequency wave propagation with angular frequency $\omega = 2\pi f$, where f is the ordinal frequency. We use the ansatz $p(x,t) = \operatorname{Re}\{\tilde{p}_\omega(x) \mathrm{e}^{\mathrm{i}\omega t}\}$ and solve the following boundary-value problem [31] for the

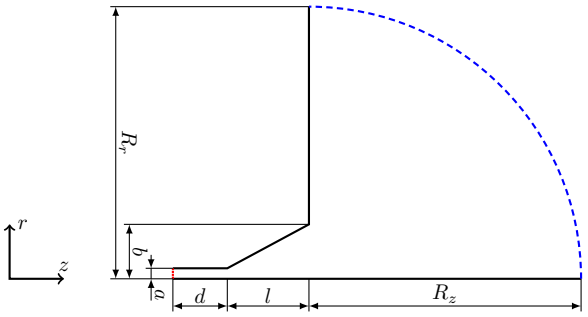

FIG. 6.1. *Cross-section of the cylindrically symmetric geometry used for the initial computations.*

complex amplitude function $\tilde{p}_\omega$:

$$\begin{aligned}
\frac{\partial}{\partial r}\left(\frac{1}{r}\frac{\partial \tilde{p}_\omega}{\partial r}\right) + \frac{\partial}{\partial z}\left(\frac{1}{r}\frac{\partial \tilde{p}_\omega}{\partial z}\right) + k^2 r \tilde{p}_\omega &= 0, && \text{in } \Omega^{(2\mathrm{D})},\\
\left(\mathrm{i}k\tilde{p}_\omega + \frac{1}{R}\right)\tilde{p}_\omega + \frac{\partial \tilde{p}_\omega}{\partial n} &= 0, && \text{on } \Gamma^{(2\mathrm{D})}_{\text{out}},\\
\mathrm{i}k\tilde{p} + \frac{\partial \tilde{p}_\omega}{\partial n} &= 2\mathrm{i}kA, && \text{on } \Gamma^{(2\mathrm{D})}_{\text{in}},\\
\frac{\partial \tilde{p}_\omega}{\partial n} &= 0, && \text{on } \Gamma^{(2\mathrm{D})}_{\text{horn}} \cup \Gamma^{(2\mathrm{D})}_{\text{symm}},
\end{aligned} \tag{6.1}$$

where $k = \omega/c$. The boundary conditions on $\Gamma^{(2\mathrm{D})}_{\text{in}}$ and $\Gamma^{(2\mathrm{D})}_{\text{out}}$ are frequency-domain analogues of characteristic boundary conditions used in the DG code at corresponding boundaries. The condition on $\Gamma^{(2\mathrm{D})}_{\text{in}}$ imposes a planar right-going wave with amplitude A while absorbing planar left going waves. At $\Gamma^{(2\mathrm{D})}_{\text{out}}$, the boundary condition absorbs any outgoing waves propagating in the normal direction with respect to the boundary. The reflection coefficient is given by

$$R^{(2D)}_\omega = \frac{2}{a^2 A}\int_{\Gamma^{(2\mathrm{D})}_{\text{in}}} r(\tilde{p}_\omega - A)\, d\Gamma. \tag{6.2}$$

For the 3D time domain DG computation, we use a truncated sinc pulse as input signal,

$$g(t) = \frac{\sin\left(2\pi f_s(t-t_c)\right)}{2\pi f_s(t-t_c)} \sin\left(2\pi f_c(t-t_c)\right) w(t, t_c), \tag{6.3}$$

where t_c is the time around which the pulse is centered, f_c is the desired center frequency, f_s is the half bandwidth of the signal, and $w(t, t_c)$ is a window function. Here, we set $t_c = 3/(2f_s)$ and use the Hamming window function

$$w(t, t_c) = \begin{cases} 0.54 + 0.46\cos\left(\frac{\pi(t-t_c)}{t_c}\right), & \text{for } t \in [0, 2t_c],\\ 0, & \text{otherwise.}\end{cases} \tag{6.4}$$

Without a window function, the spectrum of the time-infinite sinc pulse is flat within $[f_c - f_s, f_c + f_s]$ and zero outside. The use of a window function converts the infinite

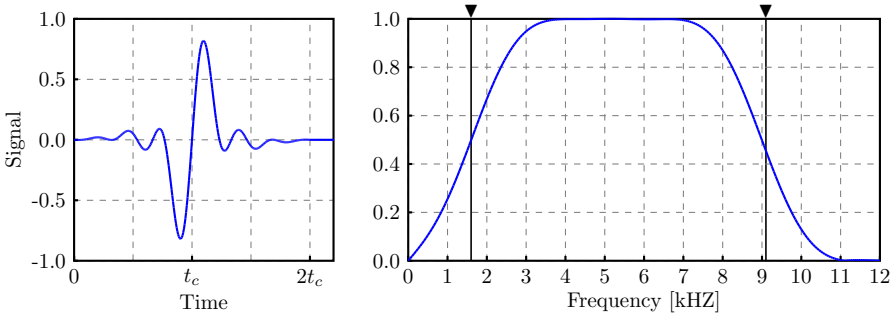

FIG. 6.2. *Left: The input signal as function of time. Right: the magnitude spectrum of the input signal for $f_c = 5.3$ kHz, $f_s = 3.7$ kHz, and $t_c = 3/7400$ s. The solid vertical lines mark the frequencies $f_c \pm f_s$ that limits the frequency range in the following figures showing the reflection spectra.*

signal to a signal of finite duration but also impacts the spectrum. In all numerical experiments using the time domain solver, we use an input signal with parameters $f_c = 5.3$ kHz and $f_s = 3.7$ kHz. Figure 6.2 illustrates the input signal as function of time (left diagram) and its normalized magnitude spectrum computed by the Discrete Fourier Transform (DFT) (right diagram).

For the baseline 2D Comsol simulations, the radius of the computational domain is $R = R_z = R_r = 1500$ mm, and we use continuous, piecewise quadratic elements on a triangular mesh with maximum side length 10 mm, which yields 97,769 unknowns for the linear system. We carry out the 3D time domain verification simulations on a cylindrical symmetric horn model in quarter symmetry, using discontinuous, piecewise linear elements on two different unstructured tetrahedral meshes, a fine resolution and a standard resolution mesh. The fine resolution mesh uses $R_z = 240$ mm, $R_r = 220$ mm and consists of $46,534$ elements, which yields a total of $(3+1) \cdot 4 \cdot 46,534 = 744,576$ unknowns per time step. The shortest edge in the mesh is 1.31 mm, the longest is 55.72 mm, and the average is 6.97 mm. As a comparison, note that the wavelength at 9 kHz is about 38 mm. For the fine resolution mesh, we use the end time $T = 18$ ms and the time step $dt = 6.25 \cdot 10^{-7}$. The standard resolution mesh uses $R_z = 80$ mm and $R_r = 140$ mm and consists of 8,356 elements, which yields 133,696 unknowns per time step. The shortest edge in this mesh is 2.51 mm, the longest edge is 36.16 mm and the average is 9.22 mm. Here, the end time $T = 4.5$ ms and the time step $dt = 2.5 \cdot 10^{-6}$. The standard resolution mesh is also the starting mesh for the optimization.

The initial 3D experiments focus on studying the transient behavior of the wave propagation and the decay of energy inside the domain. For our input signal, these experiments confirm that the acoustic energy inside the domain is exponentially decreasing, and we conclude that after about 4 ms—corresponding approximately to 10 t_c—the energy inside the computational domain is less then 10^{-6} of the energy of the input pulse. (Here, the energy inside the computational domain is evaluated as the difference between the numerically evaluated left- and right-hand sides of energy balance (3.3).) We also experimented with different time steps for the implicit time stepper and found that the above mentioned $dt = 2.5 \cdot 10^{-6}$ provides a good trade-off between computational effort and accuracy for the standard resolution mesh.

During the time domain simulations, we record the outgoing signal at Γ_{in}. After the simulation is complete, we compute the spectrum of the outgoing signal using the

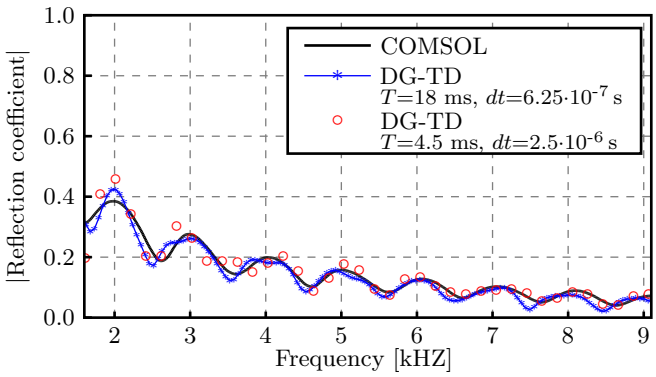

FIG. 6.3. *Magnitude reflection spectra in the range 1.6–9.1 kHz for the cylindrical symmetric horn depected in Figure 6.1 with parameters* $a = 19.3$ *mm,* $b = d = 100$ *mm, and* $l = 150$ *mm. Solid black line: Comsol Multiphysics using FD-FEM in 2D cylindrical symmetry,* 10 *Hz frequency spacing. Line with asterisks: our 3D TD-DG code, fine resolution. Circular markers: our 3D TD-DG code, standard resolution.*

DFT. The reflection coefficient spectrum at the horn's throat can then be computed by pointwise division of the Fourier coefficients of the input signal and the reflected signal. Figure 6.3 shows the magnitude of the reflection coefficient versus frequency computed by Comsol Multiphysics for the cylindrically symmetric frequency domain setup (solid line) and by our Discontinuous Galerkin 3D time domain method on the two different meshes. The difference between the two resolution cases for our DG solver, measured in terms of the point-wise absolute difference in the magnitude reflection spectra within the range 1.6–9.1 kHz is at most in the order of 10^{-2}. Both spectra, the one computed by the three dimensional time domain solver and the reference cylindrical-symmetric frequency-domain solver, agree at the upper part of the frequency range. For the lower frequencies, the spectra computed by using full 3D time domain method have larger variations than the spectrum computed by the 2D solver. The overall trends, the average decay rate with increasing frequency and the distance between peaks and valleys in the frequency spectrum remains similar for all simulations.

7. Optimization.

7.1. Preliminaries. When using a boundary representation for the shape derivative, a steepest descent algorithm for the shape optimization problem at hand can simply be implemented by

$$\Gamma_{\text{horn}}^{k+1} = \{x - \epsilon \cdot G(x) \cdot n(x) : x \in \Gamma_{\text{horn}}^{k}\}, \tag{7.1}$$

where ϵ is the step length of the gradient descent scheme, k denotes the iteration counter, and the normal derivative of the objective with respect to shape perturbations can be identified from expression (A.22), that is

$$G(x) = \int_0^T c \ \text{div}\left(p(t,x)\, u^*(t,x)\right) \, dt. \tag{7.2}$$

The adjoint variable u^* is calculated automatically and consistently by using Dolfin-Adjoint [14], which is modified such that the solution (u^*, p^*) of the discrete adjoint

process can be passed efficiently into our continuous gradient expression. Due to the boundary formulation, no additional calculations, such as the potentially very costly derivative of the mesh deformation process, are necessary. Any mesh deformation or re-meshing approach can be used, and they are interchangeable without the need to consider additional derivatives.

However, there are some geometric considerations that have not been addressed so far. First, we would like to steer the optimization towards smooth updates in order not to be trapped in local optima with bad performance [3] and in order to obtain manufacturable shapes. Secondly, we would like the horn to attach properly to the waveguide and end at a prescribed mouth shape. The latter condition prevents the optimization to gradually elongate the horn; generally, the longer the horn is, the easier it is to reduce the reflections, particularly in the low end of the target spectrum. Both these conditions can be be addressed simultaneously by calculating a smoothed descent direction G_s through the solution of

$$\begin{aligned} (-\delta\Delta_\Gamma + I)\cdot G_s &= G \qquad \text{on } \Gamma_{\text{horn}}, \\ G_s &= 0 \qquad \text{on } \partial\Gamma_{\text{horn}}, \end{aligned} \tag{7.3}$$

where Δ_Γ denotes the surface or tangential Laplacian, I is the identity and $\delta = 0.1$ is a parameter controlling the amount of gradient smoothing. Since the left side operator in equation (7.3) is positive definite, G_s is a descent direction if G is. More details on the effect of this gradient smoothing procedure can for example be found in [2, 27, 30]. The zero Dirichlet boundary condition in problem (7.3) is applied for nodes on the throat interface between horn and waveguide as well as for nodes on edges constituting the mouth, fixing those edges as discussed above.

Although the use of G_s in the optimization algorithm yields smooth updates and forces the horn to attach to the throat and the mouth, it does not necessarily lead to a good discretization of the unknown surface, meaning that very often surface nodes start to cluster, thereby creating a poor discretization and low quality DG mesh, possibly with inverted surface elements. The descent direction (A.22) is invariant under tangential modifications of V. Therefore, we can use the excess degree of freedom in the tangent plane to re-parametrize the discretization of the surface by moving nodes in tangential direction $r_1(x)\cdot\tau_1(x) + r_2(x)\cdot\tau_2(x)$, where $\tau_i(x)$ describes a consistent choice of basis vectors of the tangent plane at x and $r_i(x) \in \mathbb{R}$, such that a locally even spacing of vertices is achieved in each optimization iteration. Such a tangential re-parameterization is achieved by successively moving the surface vertices to the centroid of the corresponding Voronoi cell of the dual mesh, projected into the tangent plane. Because the Centroidal Voronoi Tesselation (CVT) can be interpreted as the dual of the Delaunay triangulation [9, 12], this approach can be thought of as turning the Delaunay remeshing procedure into a mesh deformation scheme by only relocating nodes, but not changing connectivity. More information on the reparameterization and mesh deformation approach can be found in [25]. After insuring the quality of the surface tessellation, the volume mesh is made to match the new horn boundary by solving a non-coupled component-wise Laplacian with a dampening coefficient of 0.1

Summarizing the above, we conduct a gradient descent based on the algorithm

$$\Gamma_{\text{horn}}^{k+1} = \{x - \epsilon\cdot G_s(x)\cdot n(x) + r_1(x)\cdot\tau_1(x) + r_2(x)\cdot\tau_2(x) : x \in \Gamma_{\text{horn}}^k\}.$$

As a stopping criterion, we use the size of the $L^2(\Gamma_{\text{horn}})$ of the smoothed gradient, a condition that yields a first-order necessary condition, including the geometric constraints at throat and mouth, and that also measures the actual deformation not including the tangential repair.

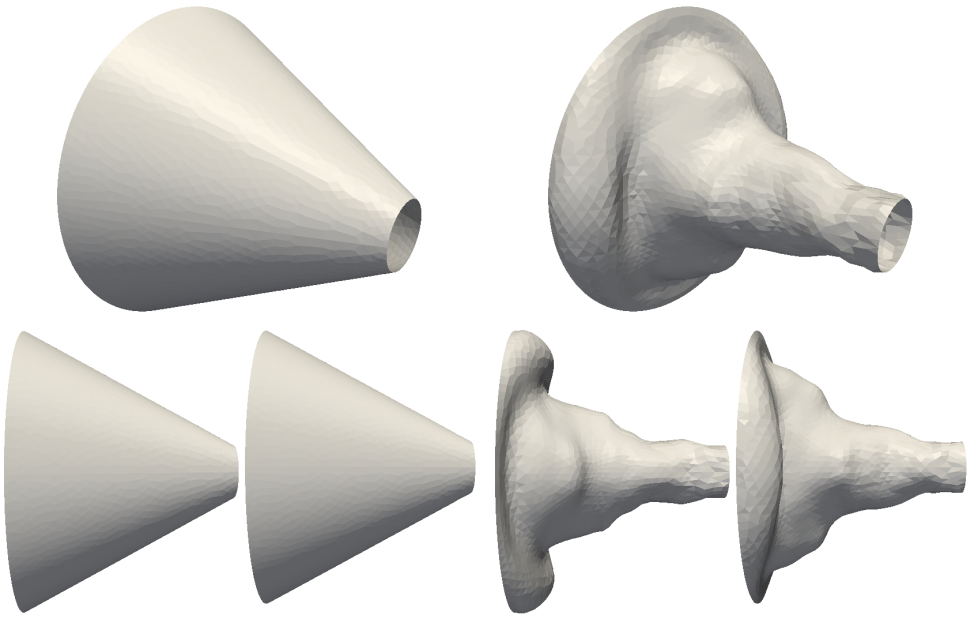

FIG. 7.1. *Isoperimetric, top and side view of the circular test-case.*

7.2. Numerical Results. We consider two different test cases for optimization. The first case involves the same circular geometry of the throat and mouth as used for the verification computations in Section 6, and the starting geometry is the conical horn of the verification. The second case involves a horn that blends a circular throat of 19.3 mm radius (same as in the verification) into an elliptic mouth with the two half-axis 100 mm and 60 mm, respectively. The blending is linear for the starting geometry. The sinc-pulse—and therefore the spectrum to optimize for—is the same as for the validation calculations above.

The quarter-section of the horn for the first test case has 698 unknown points on the surface, which are the design unknowns to be moved in both normal and tangential direction subject to the throat and mouth constraints build into the smoother (7.3). The initial conical horn results in an objective function value of $J = 2.0563 \cdot 10^{-4}$. After optimization an objective function value of $J = 5.3053 \cdot 10^{-6}$ is achieved. Figure 7.1 shows the initial as well as the optimized horn shapes. The apparent loss of cylindrical symmetry is not surprising, because the unstructured initial tetrahedral mesh is not perfectly rotationally symmetric. Thus, already after the first iteration of the optimization procedure the design cannot be expected to be symmetric. Moreover, the shape optimization problem is intrinsically non-linear and the solution with radial symmetry seems not to be stable under small perturbations. Special measures, such as a explicit enforcement of symmetry, would need to be taken in order to obtain a rotationally symmetric solution for this case.

However, the focus of this work is not to enforce a rotationally symmetric solution but solving a truly three dimensional problem. The second test case concerns an elliptically shaped mouth, which is of much more importance with respect to actual applications with a desired farfield radiation pattern. The elliptic geometry is determined by 562 nodes on the surface. Here, we manage to reduce the objective function

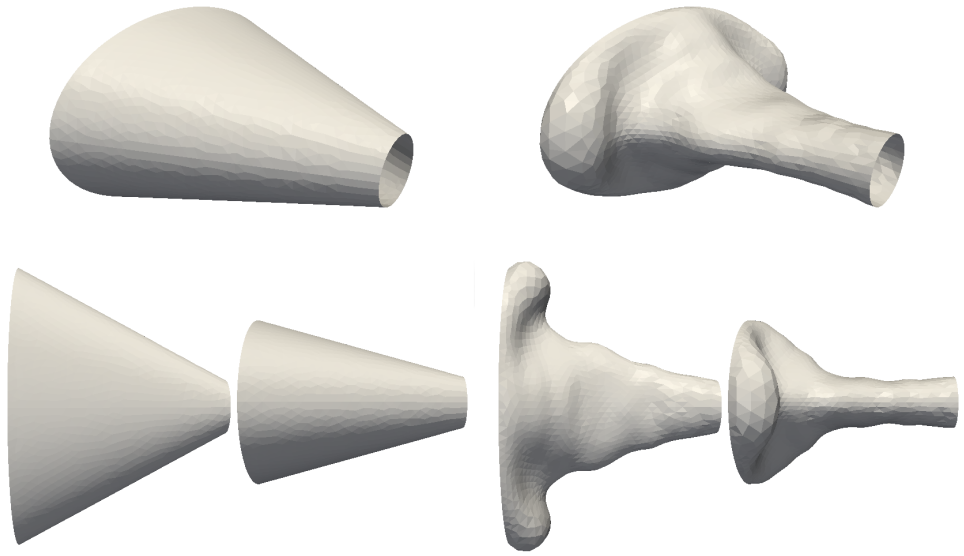

FIG. 7.2. *Isoperimetric, top and side view of the elliptic test-case.*

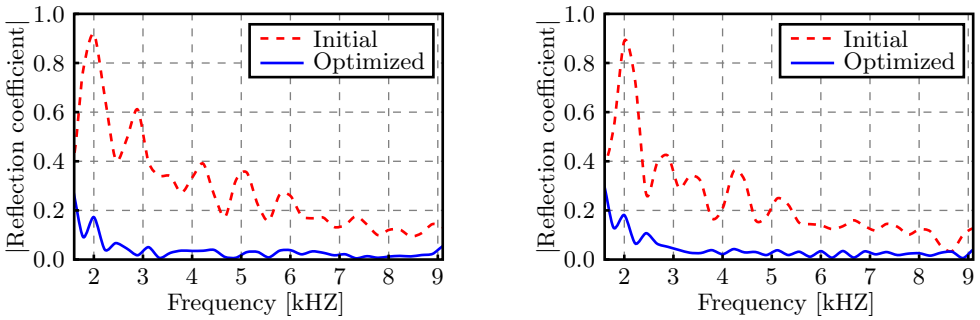

FIG. 7.3. *Magnitude reflection spectra of the initial (dashed lines) as well as the optimized horns (solid lines) corresponding to the test cases with circular (left) and elliptic (right) mouths.*

from $1.5133 \cdot 10^{-4}$ to $7.2369 \cdot 10^{-6}$ after 1160 iterations. Figure 7.2 shows the initial as well as the optimized horn shapes from the optimization of a horn with an elliptic mouth.

Magnitude reflection spectra for both test-cases are shown in Figure 7.3. The spectrum of the optimized horns with their non-intuitive shape is a substantial improvement over the initial geometry over the whole frequency band prescribed by the incoming sinc-pulse with some frequencies actually having a reflection coefficient of almost zero. By comparing the optimized horn shapes in Figures 7.1 and 7.2, we see that they share the same major features. Figure 7.4 shows the effective radii, that is the radii that would give cylindrically symmetric horns of the same cross sectional area as the considered shapes, of the initial and optimized horns for both test cases. The optimized horns' cross sectional area is strictly increasing in the axial direction and avoids the sharp edge at the throat, which the initial horns exhibit. The

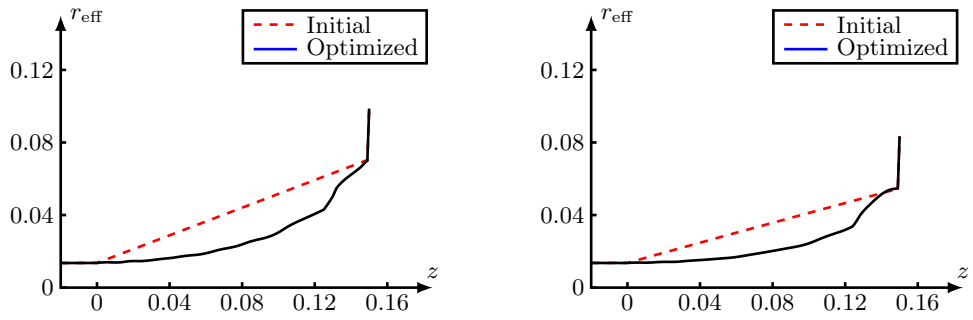

FIG. 7.4. *Effective radii of the initial (dashed lines) as well as the optimized horns (solid lines) corresponding to the optimization runs with the circular (left) and elliptic (right) initial geometry.*

behavior of the effective radii, for both the optimized horns, changes character a few centimeters from the horn mouth (approximately at $z = 0.13$ m) where the effective radius quickly increases and then levels out; this feature is particularly marked for the elliptic test-case. This is most likely an interesting end effect that stems from the fixed rim of the horn mouth. A closer look at the three dimensional shapes reveals that the deformations of the horn close to the outer rim are larger for the optimized horn with a circular mouth. One possible explanation of the shape close to the rim is simply that the performance could be improved by elongating the horn by moving interior parts of the flare along the axial direction while keeping the rim fixed.

8. Discussion and Outlook. To the best of our knowledge, this is the first time that numerical shape optimization has been used for detailed design of an acoustic horn using full 3D time domain modeling. The characteristic decomposition of the acoustic power density is a key ingredient in our approach; it is used both to define the objective function for the optimization and to obtain stable numerical fluxes in the numerical method. Another key ingredient is the surface representation of the objective function gradient, which limits the need for storage of time histories of the primal and adjoint variables to the design boundary. The alternative to rely on exact gradients to the discrete objective function would involve the time history of the fields throughout the domain, which would require excessive storage, and would also necessitate access to derivatives of the mesh deformation scheme. The software for the acoustic analysis as well as the adjoint solver needed for sensitivity calculations are semi-automatically generated by the FEniCS and Dolfin–Adjoint frameworks. Smoothness requirements on the design updates as well as the fixed throat and mouth geometries are imposed through design by using the Laplace–Beltrami operator. The corresponding solver, as well as the solver for the mesh deformation routine, were also generated through the FEniCS framework.

Being able to optimize complex three dimensional geometries in a time-domain formulation will enable the consideration of more challenging objective functions in the future, such as impedance matching to a specific source and requirements on the far field radiation pattern.

Appendix A. Sensitivity Analysis.

A.1. Basic formulas. Let Ω denote an open and bounded domain in $\mathbb{R}^3$, and let $\Gamma \subset \partial\Omega$. We will differentiate integrals of the types

$$J_1(\Omega) = \int_\Omega f \, dx, \qquad J_2(\Omega) = \int_\Gamma h \, d\Gamma. \tag{A.1}$$

with respect to domain variations generated by a smooth vector field $V : \mathbb{R}^3 \to \mathbb{R}^3$. A family of deformed domains Ω^ϵ and surfaces Γ^ϵ, parametrized by $\epsilon \geq 0$, are generated by the formula $x_\epsilon = x + \epsilon V(x)$ for $x \in \Omega$ or $x \in \Gamma$. We consider families of functions f_ϵ and h_ϵ defined on Ω^ϵ and Γ^ϵ, where $f = f_0$ and $h = h_0$, and define shape derivatives of integrals (A.1) as

$$dJ_1(\Omega)[V] = \lim_{\epsilon\to 0^+} \frac{1}{\epsilon}\Big(\int_{\Omega^\epsilon} f_\epsilon \, dx - \int_\Omega f \, dx\Big) =: \frac{d^+}{d\epsilon}\int_{\Omega^\epsilon} f_\epsilon \, dx\Big|_{\epsilon=0}, \tag{A.2a}$$

$$dJ_2(\Omega)[V] = \lim_{\epsilon\to 0^+} \frac{1}{\epsilon}\Big(\int_{\Gamma^\epsilon} h_\epsilon \, d\Gamma - \int_\Gamma h \, d\Gamma\Big) =: \frac{d^+}{d\epsilon}\int_{\Gamma^\epsilon} h_\epsilon \, d\Gamma\Big|_{\epsilon=0}, \tag{A.2b}$$

if the limits exist. The *material derivate* of function families f_ϵ and h_ϵ at $\epsilon = 0$ are defined as

$$\dot{f}[V](x) = \lim_{\epsilon\to 0^+} \frac{f_\epsilon\big(x + \epsilon V(x)\big) - f(x)}{\epsilon}, \tag{A.3a}$$

$$\dot{h}[V](x) = \lim_{\epsilon\to 0^+} \frac{h_\epsilon\big(x + \epsilon V(x)\big) - h(x)}{\epsilon}, \tag{A.3b}$$

if the limits exist, and the *shape derivative* of the families are defined as

$$f'[V] = \dot{f}[V] - \big\langle V, \nabla f\big\rangle, \tag{A.4a}$$

$$h'[V] = \dot{h}[V] - \big\langle V, \nabla h\big\rangle. \tag{A.4b}$$

Remark A.1. An often used alternative characterization of the shape derivative is the partial derivatives with respect to ϵ; that is, for fixed x, we have

$$f'[V](x) = \lim_{\epsilon\to 0} \frac{f_\epsilon(x) - f(x)}{\epsilon}, \tag{A.5a}$$

$$h'[V](x) = \lim_{\epsilon\to 0} \frac{h_\epsilon(x) - h(x)}{\epsilon}, \tag{A.5b}$$

which can be obtained by a Taylor expansion of f_ϵ and h_ϵ in definitions (A.3). However, a complicating factor with characterizations (A.5) is that the arguments of f_ϵ of h_ϵ in expressions (A.5) are not necessarily in the domains of definition Ω^ϵ, Γ^ϵ of the functions.

Sokolowski & Zolesio [29, § 2.31] prove the following formula for shape derivative (A.2a) under the assumptions that Ω is of class C^k, $k \geq 1$, and that f, $f'[V]$, and $\|\nabla f\|$ are all in $L^1(\Omega)$,

$$dJ_1(\Omega)[V] = \int_\Omega f'[V] + \operatorname{div}(Vf)\, dx = \int_\Omega f'[V]\, dx + \int_{\partial\Omega} \langle V, n\rangle f \, d\Gamma \tag{A.6}$$

We will consider shape derivate (A.2b) in the three cases

(i) $\langle V, n\rangle \equiv 0$ on $\Gamma \subset \partial\Omega$,
(ii) $h(x) = \langle \tilde{h}(x), n(x)\rangle$, $\Gamma = \partial\Omega$, n is the outward-directed normal field on Γ, and $\tilde{h}$ is the trace of a vector-valued function in Ω whose divergence satisfies the conditions for f assumed for formula (A.6).
(iii) Conditions as for case (ii) but $\Gamma \subset \partial\Omega$ such that $\langle V, n\rangle \equiv 0$ on $\partial\Omega \setminus \Gamma$.

For these cases, the formula

$$dJ_2(\Omega)[V] = \begin{cases} \displaystyle\int_\Gamma h'[V]\, d\Gamma & \text{in Case (i),} \\ \displaystyle\int_\Gamma \langle \tilde{h}'[V], n\rangle + \langle V, n\rangle \operatorname{div} \tilde{h}\, d\Gamma & \text{in Cases (ii) and (iii)} \end{cases} \tag{A.7}$$

holds, where div $\tilde{h}$ inside the boundary integral denotes the trace on Γ of the divergence of $\tilde{h}$ in Ω. In case (i), $\Gamma^\epsilon = \Gamma$, so the formula follows immediately by definitions (A.3b) and (A.4b) as long as $h'[V]$ exists and is integrable. In case (ii), the divergence theorem and the substitution $f = \operatorname{div} \tilde{h}$ turns integral J_2 into a domain integral of the J_1 type. Formula (A.7) then follows from expression (A.6) using the divergence theorem and the fact that the shape derivative and the spatial gradient commute. The formula for case (iii) follows from cases (i) and (ii).

Remark A.2. Due to the particular integral form of the state equation used in § A.2, the conditions of Cases (i) and (ii) will be satisfied, and shape derivate formulas (A.6) and (A.7) are all that are needed. However, if the hard wall boundary condition on Γ_{horn} is imposed in a different way, for instance through an upwinding flux together with a remote mirrored state, as discussed in § 5, the linear structure assumed in Cases (ii) and (iii) does not hold, and a formula admitting a more general form of the integrand h in integral J_2 is needed. A more general form is obtained by considering a family, parameterized by ϵ, of functions $\hat{h}_\epsilon$ defined on $\overline{\Omega}^\epsilon \times \overline{\Omega}^\epsilon$, and defining the integrand in J_2 to be $h_\epsilon(x_\epsilon) = \hat{h}_\epsilon(x_\epsilon, n_\epsilon(x_\epsilon))$ for $x_\epsilon \in \Gamma^\epsilon$. The shape derivative formula then becomes

$$dJ_2(\Omega)[V] = \int_\Gamma \hat{h}'[V] + \langle V, n\rangle \Big(\big\langle \nabla \hat{h}, n\big\rangle + \kappa\big(\hat{h} - \langle \nabla_y \hat{h}, n\rangle\big) + \operatorname{div}_\Gamma \big(\nabla_y \hat{h}\big)\Big)\, d\Gamma, \tag{A.8}$$

where κ is the local mean curvature, ∇ and $\operatorname{div}_\Gamma$ the gradient and the tangential divergence with respect to the first argument of $\hat{h}$, and ∇_y the gradient with respect to the second argument. Formula (A.8) is a special case of Lemma 3.3.14 in the first author's Ph. D. thesis [24]. To the best of our knowledge, this formula does not appear anywhere else in the open literature.

A.2. Shape derivatives and the adjoint system. We consider the objective function (3.4), where u, p satisfy initial–boundary-value problem (3.1). We require that the vector field V that generates the domain variations, as described above, vanishes on $\partial\Omega \setminus \Gamma_{\text{horn}}$. This field V will generate a family of perturbed domains Ω^ϵ for which the horn boundary $\Gamma^\epsilon_{\text{horn}}$ is perturbed. However, the rest of the boundary, $\partial\Omega \setminus \Gamma^\epsilon_{\text{horn}}$, will be fixed independent of ϵ.

Differentiating objective function (3.4), using formula (A.7), and utilizing that V vanishes on Γ_{in}, we get

$$dJ(\Omega)[V] = \int_0^T \int_{\Gamma_{\text{in}}} \big(p + c\langle u, n\rangle\big)\big(p'[V] + c\langle u'[V], n\rangle\big)\, d\Gamma\, dt. \tag{A.9}$$

In order to continue, we need to determine how the shape derivatives $p'[V]$, $u'[V]$ in expression (A.9) depend on V. We will therefore differentiate the state equation with respect to domain perturbations. To prepare for the use of formulas (A.6) and (A.7), we first rewrite state equation (3.1) in the integral form

$$\begin{aligned} c\int_\Omega \langle v, \partial_t u + \nabla p\rangle \,dx + \frac{1}{c}\int_\Omega q(\partial_t p + c^2 \operatorname{div} u)\,dx - c\int_{\Gamma_\mathrm{s}} q\langle u, n\rangle \,d\Gamma \\ + \frac{1}{2}\int_{\Gamma_\mathrm{inout}} (q - c\langle v, n\rangle)(p - c\langle u, n\rangle)\,d\Gamma = \int_{\Gamma_\mathrm{in}} (q - c\langle v, n\rangle) g \,d\Gamma, \end{aligned} \tag{A.10}$$

where $\Gamma_\mathrm{s} = \Gamma_\mathrm{wall} \cup \Gamma_\mathrm{symm}$ and $\Gamma_\mathrm{inout} = \Gamma_\mathrm{in} \cup \Gamma_\mathrm{out}$, and where v and q are arbitrary smooth test functions.

Remark A.3. It is immediate, by inspection, that integral form (A.10) is *consistent* with system (3.1); that is, solutions to system (3.1) satisfy expression (A.10) for any smooth test functions. Moreover, integral form (A.10) is designed to satisfy a *stability* property, namely that the acoustic energy decreases with time when no input is provided to the systems. That is, for $g = 0$,

$$\frac{c}{2}\frac{d}{dt}\int_\Omega |u|^2\,dx + \frac{1}{2c}\frac{d}{dt}\int_\Omega p^2\,dx + \frac{1}{2}\int_{\Gamma_\mathrm{inout}} \left(p^2 + c^2\langle u, n\rangle^2\right) d\Gamma = 0, \tag{A.11}$$

which can be seen by substituting $v = u$, $q = p$ in equation (A.10), using the product rule, and integrating by parts.

Let $v = u^*$, $q = -p^*$ in equation (A.10), for some arbitrary smooth functions u^* and p^* (these will later be chosen to satisfy the adjoint equation). Integrating in time over an interval $(0, T)$ yields

$$\begin{aligned} 0 = c\int_0^T\!\!\int_\Omega \langle u^*, \partial_t u + \nabla p\rangle \,dx\,dt - \frac{1}{c}\int_0^T\!\!\int_\Omega p^*(\partial_t p + c^2 \operatorname{div} u)\,dx\,dt \\ + c\int_0^T\!\!\int_{\Gamma_\mathrm{s}} p^*\langle u, n\rangle \,d\Gamma\,dt - \frac{1}{2}\int_0^T\!\!\int_{\Gamma_\mathrm{inout}} (p^* + c\langle u^*, n\rangle)(p - c\langle u, n\rangle)\,d\Gamma\,dt \\ + \int_0^T\!\!\int_{\Gamma_\mathrm{in}} (p^* + c\langle u^*, n\rangle) g \,d\Gamma\,dt. \end{aligned} \tag{A.12}$$

Now assume that the domain Ω is perturbed by domain variations generated by a vector field V, chosen as described above. We denote by subscript ϵ on the state and co-state variables the solutions associated with the perturbed domain Ω^ϵ. Differentiating

equation (A.12) with respect to a domain variation generated by V results in

$$\begin{aligned}
0 = {} & c\frac{d^+}{d\epsilon}\int_0^T\int_{\Omega^\epsilon}\langle u_\epsilon^*, \partial_t u_\epsilon + \nabla p_\epsilon\rangle\, dx\, dt\Big|_{\epsilon=0} \\
& - \frac{1}{c}\frac{d^+}{d\epsilon}\int_0^T\int_{\Omega^\epsilon} p_\epsilon^*(\partial_t p_\epsilon + c^2 \mathrm{div}\, u_\epsilon)\, dx\, dt\Big|_{\epsilon=0} + c\frac{d^+}{d\epsilon}\int_0^T\int_{\Gamma_{\mathrm{s}}^\epsilon} p_\epsilon^*\langle u_\epsilon, n\rangle\, d\Gamma\, dt\Big|_{\epsilon=0} \\
& - \frac{1}{2}\frac{d^+}{d\epsilon}\int_0^T\int_{\Gamma_{\mathrm{inout}}} (p_\epsilon^* + c\langle u_\epsilon^*, n\rangle)(p_\epsilon - c\langle u_\epsilon, n\rangle)\, d\Gamma\, dt\Big|_{\epsilon=0} \\
& + \frac{d^+}{d\epsilon}\int_0^T\int_{\Gamma_{\mathrm{in}}} (p_\epsilon^* + c\langle u_\epsilon^*, n\rangle) g\, d\Gamma\, dt\Big|_{\epsilon=0}.
\end{aligned} \tag{A.13}$$

Applying formulas (A.6) and (A.7), where case (i) applies to Γ_{inout} and Γ_{in} and case (iii) to Γ_{s}, together with the product rule of differentiation and the fact that the shape derivative commutes with time and spatial differentiation yields that expression (A.13) expands to

$$\begin{aligned}
0 = {} & c\int_0^T\int_\Omega \langle u^{*\prime}, \partial_t u + \nabla p\rangle\, dx\, dt - \frac{1}{c}\int_0^T\int_\Omega p^{*\prime}(\partial_t p + c^2 \mathrm{div}\, u)\, dx\, dt \\
& + c\int_0^T\int_{\Gamma_{\mathrm{s}}} p^{*\prime}\langle u, n\rangle\, d\Gamma\, dt - \frac{1}{2}\int_0^T\int_{\Gamma_{\mathrm{inout}}} (p^{*\prime} + c\langle u^{*\prime}, n\rangle)(p - c\langle u, n\rangle)\, d\Gamma\, dt \\
& + \int_0^T\int_{\Gamma_{\mathrm{in}}} (p^{*\prime} + c\langle u^{*\prime}, n\rangle) g\, d\Gamma\, dt \\
& + c\int_0^T\int_\Omega \langle u^*, \partial_t u' + \nabla p'\rangle\, dx\, dt - \frac{1}{c}\int_0^T\int_\Omega p^*(\partial_t p' + c^2 \mathrm{div}\, u')\, dx\, dt \\
& + c\int_0^T\int_{\Gamma_{\mathrm{s}}} p^*\langle u', n\rangle\, d\Gamma\, dt - \frac{1}{2}\int_0^T\int_{\Gamma_{\mathrm{inout}}} (p^* + c\langle u^*, n\rangle)(p' - c\langle u', n\rangle)\, d\Gamma\, dt \\
& + c\int_0^T\int_{\Gamma_{\mathrm{horn}}} \langle V, n\rangle\langle u^*, \partial_t u + \nabla p\rangle\, d\Gamma\, dt \\
& - \frac{1}{c}\int_0^T\int_{\Gamma_{\mathrm{horn}}} \langle V, n\rangle p^*(\partial_t p + c^2 \mathrm{div}\, u)\, d\Gamma\, dt + c\int_0^T\int_{\Gamma_{\mathrm{horn}}} \langle V, n\rangle \mathrm{div}\,(u p^*)\, d\Gamma\, dt,
\end{aligned} \tag{A.14}$$

where the dependency on V of the shape derivatives have been surpressed for brevity.

The first five terms in expression (A.14) vanish identically since u, p satisfy equation (A.12). Moreover, provided that u, p, and Γ_{horn} are regular enough, terms 10 and 11 in expression (A.14) will also vanish identically, due to state equation (3.1).

(A sufficient regularity condition is that u and p as well as their derivatives can be continuously extended up to Γ_{horn}.) Reducing these terms from expression (A.14) yields

$$\begin{aligned}0 = c\int_0^T\int_\Omega \langle u^*, \partial_t u' + \nabla p'\rangle \,dx\,dt - \frac{1}{c}\int_0^T\int_\Omega p^*(\partial_t p' + c^2 \operatorname{div} u')\,dx\,dt \\ + c\int_0^T\int_{\Gamma_{\text{s}}} p^*\langle u', n\rangle \,d\Gamma\,dt - \frac{1}{2}\int_0^T\int_{\Gamma_{\text{inout}}} (p^* + c\langle u^*, n\rangle)(p' - c\langle u', n\rangle)\,d\Gamma\,dt \\ + c\int_0^T\int_{\Gamma_{\text{horn}}} \langle V, n\rangle \operatorname{div}(up^*)\,d\Gamma\,dt.\end{aligned} \tag{A.15}$$

By integrating $\langle u^*, \partial_t u'\rangle$ by parts in time and integrating $\langle u^*, \nabla p'\rangle$ by parts in space, we can write the first term in expression (A.15) as

$$\begin{aligned}c\int_0^T\int_\Omega \langle u^*, \partial_t u' + \nabla p'\rangle \,dx\,dt = c\int_\Omega \langle u'(T), u^*(T)\rangle\,dx - c\int_0^T\int_\Omega \langle u', \partial_t u^*\rangle\,dx\,dt \\ + c\int_0^T\int_{\partial\Omega} p'\langle u^*, n\rangle\,d\Gamma\,dt - c\int_0^T\int_\Omega p'\operatorname{div} u^*\,dx\,dt,\end{aligned} \tag{A.16}$$

where we have used that $u'|_{t=0}$ and $p'|_{t=0}$ vanish due to the homogeneous initial conditions for state equation (3.1). Similarly, by integrating $p^*\partial_t p'$ by parts in time and integrating $p^*\operatorname{div} u'$ by parts in space, the second term in expression (A.15) becomes

$$\begin{aligned}\frac{1}{c}\int_0^T\int_\Omega p^*(\partial_t p' + c^2\operatorname{div} u')\,dx\,dt = \frac{1}{c}\int_\Omega p'(T)p^*(T)\,dx - \frac{1}{c}\int_0^T\int_\Omega p'\partial_t p^*\,dx\,dt \\ + c\int_0^T\int_{\partial\Omega} \langle u', n\rangle p^*\,d\Gamma\,dt - c\int_0^T\int_\Omega \langle u', \nabla p^*\rangle\,dx\,dt.\end{aligned} \tag{A.17}$$

Substituting expressions (A.16) and (A.17) into expression (A.15) and recombining the terms using that $\partial\Omega = \Gamma_{\text{s}} \cup \Gamma_{\text{inout}}$, we find that

$$\begin{aligned}0 = c\int_\Omega \langle u'(T), u^*(T)\rangle\,dx + c\int_0^T\int_\Omega \langle u', -\partial_t u^* + \nabla p^*\rangle\,dx\,dt \\ - \frac{1}{c}\int_\Omega p'(T)p^*(T)\,dx - \frac{1}{c}\int_0^T\int_\Omega p'(-\partial_t p^* + c^2\operatorname{div} u^*)\,dx\,dt \\ + c\int_0^T\int_{\Gamma_{\text{s}}} p'\langle u^*, n\rangle\,d\Gamma\,dt - \frac{1}{2}\int_0^T\int_{\Gamma_{\text{inout}}} \big(p^* - c\langle u^*, n\rangle\big)\big(p' + c\langle u', n\rangle\big)\,d\Gamma\,dt\end{aligned} \tag{A.18}$$

$$+ c \int_0^T \int_{\Gamma_{\text{horn}}} \langle V, n \rangle \operatorname{div}(u p^*)\, d\Gamma\, dt.$$

So far functions p^*, u^* have been arbitrary. However, if we assume that they satisfy the adjoint system

$$\begin{aligned}
-\frac{\partial u^*}{\partial t} + \nabla p^* &= 0 && \text{in } \Omega, \text{ for } t < T,\\
-\frac{\partial p^*}{\partial t} + c^2 \operatorname{div} u^* &= 0 && \text{in } \Omega, \text{ for } t < T,\\
\frac{1}{2}\left(p^* - c\langle u^*, n\rangle\right) &= \frac{1}{2}\left(p + c\langle u, n\rangle\right) && \text{on } \Gamma_{\text{in}}, \text{ for } t < T,\\
\frac{1}{2}\left(p^* - c\langle u^*, n\rangle\right) &= 0 && \text{on } \Gamma_{\text{out}}, \text{ for } t < T,\\
\langle u^*, n\rangle &= 0 && \text{on } \Gamma_{\text{wall}} \cup \Gamma_{\text{symm}}, \text{ for } t < T,\\
u^* &\equiv 0 && \text{in } \Omega, \text{ at } t = T,\\
p^* &\equiv 0 && \text{in } \Omega, \text{ at } t = T,
\end{aligned} \tag{A.19}$$

expression (A.18) reduces to

$$\frac{1}{2} \int_0^T \int_{\Gamma_{\text{in}}} \left(p + c\langle u, n\rangle\right)\left(p' + c\langle u', n\rangle\right) d\Gamma\, dt = c \int_0^T \int_{\Gamma_{\text{horn}}} \langle V, n\rangle \operatorname{div}(u p^*)\, d\Gamma\, dt, \tag{A.20}$$

which combined with expression (A.9) means that the shape derivate can be given by the integral representation

$$dJ(\Gamma_{\text{horn}})[V] = c \int_0^T \int_{\Gamma_{\text{horn}}} \langle V, n\rangle \operatorname{div}(u p^*)\, d\Gamma\, dt. \tag{A.21}$$

Remark A.4. The shape derivative representation can also be written as

$$dJ(\Gamma_{\text{horn}})[V] = c \int_0^T \int_{\Gamma_{\text{horn}}} \langle V, n\rangle \operatorname{div}(u^* p)\, d\Gamma\, dt. \tag{A.22}$$

This alternative expression can be derived as follows:

$$\begin{aligned}
&\int_0^T \int_{\Gamma_{\text{horn}}} \langle V, n\rangle \operatorname{div}(u p^*)\, d\Gamma\, dt = \int_0^T \int_{\Gamma_{\text{horn}}} \langle V, n\rangle \left(\langle u, \nabla p^*\rangle + p^* \operatorname{div} u\right) d\Gamma\, dt\\
&= \int_0^T \int_{\Gamma_{\text{horn}}} \langle V, n\rangle \left(\langle u, \partial_t u^*\rangle - \frac{1}{c^2} p^* \partial_t p\right) d\Gamma\, dt\\
&= -\int_0^T \int_{\Gamma_{\text{horn}}} \langle V, n\rangle \left(\langle \partial_t u, u^*\rangle - \frac{1}{c^2} \partial_t p^* p\right) d\Gamma\, dt\\
&= \int_0^T \int_{\Gamma_{\text{horn}}} \langle V, n\rangle \left(\langle \nabla p, u^*\rangle + p \operatorname{div} u^*\right) d\Gamma\, dt = \int_0^T \int_{\Gamma_{\text{horn}}} \langle V, n\rangle \operatorname{div}(p u^*)\, d\Gamma\, dt,
\end{aligned} \tag{A.23}$$

where the state (3.1) and adjoint (A.19) equations have been used in the second and fourth equalities, and integration by part in time in the third equality, where also the homogeneous initial (or terminal) conditions for u, u^*, p and p^* have been exploited.

REFERENCES

[1] S. G. Amin, M. H. M. Ahmed, and H. A. Youssef, *Computer-aided design of acoustic horns for ultrasonic machining using finite-element analysis*, Journal of Materials Processing Technology, 55 (1995), pp. 254–260.

[2] E. Arian and S. Ta'asan, *Analysis of the Hessian for aerodynamic optimization: Inviscid flow*, Tech. Report 96-28, Institute for Computer Applications in Science and Engineering (ICASE), 1996.

[3] E. Bängtsson, D. Noreland, and M. Berggren, *Shape optimization of an acoustic horn*, Computer Methods in Applied Mechanics and Engineering, 192 (2003), pp. 1533–1571.

[4] R. Barbieri, N. Barbieri, and K. Fonseca de Lima, *Some applications of the PSO for optimization of acoustic filters*, Applied Acoustics, 80 (2015), pp. 62–70.

[5] M. P. Bendsøe and O. Sigmund, *Topology Optimization – Theory, Methods and Applications*, Springer, Berlin, Heidelberg, New York, 2nd ed., 2004.

[6] R. Berbieri and N. Barbieri, *Acoustic horns optimization using finite elements and genetic algorithm*, Applied Acoustics, 74 (2013), pp. 356–363.

[7] M. Berggren, *A unified discrete-continuous sensitivity analysis method for shape optimization*, in Applied and Numerical Partial Differential Equations, vol. 15 of Computational Methods in Applied Sciences, Springer Netherlands, 2010, pp. 25–39.

[8] D. J. Brackett, I. A. Ashcroft, and R. J. M. Hague, *Multi-physics optimisation of 'brass' instruments—a new method to include structural and acoustical interactions*, Structural and Multidisciplinary Optimization, (2010). Available online.

[9] L. Chen, *Mesh smoothing schemes based on optimal Delaunay triangulations*, in 13th International Meshing Roundtable, Williamsburg, VA, 2004, Sandia National Laboratories, pp. 109–120.

[10] M. Colloms, *High Performance Loudspeakers*, Wiley, sixth ed., 2005.

[11] M. C. Delfour and J.-P. Zolézio, *Shapes and Geometries. Metrics, Analysis, Differential Calculus, and Optimization*, SIAM, Philadelphia, second ed., 2011.

[12] Q. Du, V. Faber, and M. Gunzburger, *Centroidal Voronoi tessellations: Applications and algorithms*, SIAM Review, 41 (1999), pp. 637–676.

[13] B. Farhadinia, *Structural optimization of an acoustic horn*, Applied Mathematical Modeling, 36 (2012), pp. 2017–2030.

[14] P.E. Farrell, D.A. Ham, S.W. Funke, and M.E. Rognes, *Automated derivation of the adjoint of high-level transient finite element programs*, SIAM Journal on Scientific Computing, 35 (2013), pp. 369–393.

[15] J. S. Hesthaven and T. Warburton, *Nodal Discontinuous Galerkin Methods. Algorithms, Analysis, and Applications*, vol. 54 of Texts in Applied Mathematics, Springer, 2008.

[16] R. M. Hicks and P. A. Henne, *Wing design by numerical optimization*, Journal of Aircraft, 15 (1978), pp. 407–412.

[17] F. Kasolis, E. Wadbro, and M. Berggren, *Fixed-mesh curvature-parameterized shape optimization of an acoustic horn*, Structural and Multidisciplinary Optimization, 46 (2012), pp. 727–738.

[18] A. Logg, K.-A. Mardal, and G. N. Wells, eds., *Automated Solution of Differential Equations by the Finite Element Method*, Lecture Notes in Computational Science and Engineering, Springer, 2012.

[19] R. C. Morgans, A. C. Zander, C. H. Hansen, and D. J. Murphy, *EGO shape optimization of horn-loaded loudspeakers*, Optimization and Engineering, 9 (2008), pp. 361–374.

[20] P. M. Morse, *Vibration and Sound*, McGraw–Hill, 1948.

[21] D. Noreland, R. Udawalpola, and M. Berggren, *A hybrid scheme for bore design optimization of a brass instrument*, Journal of Acoustical Society of America, 128 (2010), pp. 1391–1400.

[22] D. Noreland, R. Udawalpola, P. Seoane, E. Wadbro, and M. Berggren, *An efficient loudspeaker horn design by numerical optimization: an experimental study*, Tech. Report UMINF 10.0, Department of Computing Science, Umeå University, 2009.

[23] S. W. Rienstra and A. Hirschberg, *An introduction to acoustics*. Revised and updated version of reports IWDE 92-06 and IWDE 01-03, Eindhoven University of Technology.

[24] S. Schmidt, *Efficient Large Scale Aerodynamic Design Based on Shape Calculus*, PhD thesis,

University of Trier, Germany, 2010.

[25] ———, *A two stage CVT / eikonal convection mesh deformation approach for large nodal deformations*. eprint arXiv:1411.7663 (submitted), 2014.

[26] S. Schmidt, C. Ilic, V. Schulz, and N. Gauger, *Three dimensional large scale aerodynamic shape optimization based on shape calculus*, AIAA Journal, 51 (2013), pp. 2615–2627.

[27] S. Schmidt and V. Schulz, *Impulse response approximations of discrete shape Hessians with application in CFD*, SIAM Journal on Control and Optimization, 48 (2009), pp. 2562–2580.

[28] ———, *A 2589 line topology optimization code written for the graphics card*, Computing and Visualization in Science, 14 (2011), pp. 249–256. (published online 14.08.2012).

[29] J. Sokolowski and J.-P. Zolésio, *Introduction to Shape Optimization: Shape Sensitivity Analysis*, Springer Berlin Heidelberg, 1992.

[30] S. Ta'asan, *One-shot methods for optimal control of distributed parameter systems I: Finite dimensional control*, ICASE, 91-2 (1991).

[31] R. Udawalpola and M. Berggren, *Optimization of an acoustic horn with respect to efficiency and directivity*, International Journal of Numerical Methods in Engineering, 73 (2008), pp. 1571–1606.

[32] R. Udawalpola, E. Wadbro, and M. Berggren, *Optimization of a variable mouth acoustic horn*, International Journal for Numerical Methods in Engineering, 85 (2011), pp. 591–606.

[33] E. Wadbro and M. Berggren, *Topology optimization of an acoustic horn*, Computer Methods in Applied Mechanics and Engineering, 196 (2006), pp. 429–436.

[34] E. Wadbro, R. Udawalpola, and M. Berggren, *Shape and topology optimization of an acoustic horn–lens combination*, Journal of Computational and Applied Mathematics, 234 (2010), pp. 1781–1787.

[35] B. Webb and J. Baird, *Advances in line array technology for live sound*, in Audio Engineering Society Conference: UK 18th Conference: Live Sound, 2003.